

# Artificially tailored relaxor ferroelectrics for high energy density capacitors

**Jungho Ryu** (✉ [jhryu@ynu.ac.kr](mailto:jhryu@ynu.ac.kr))

Yeungnam University <https://orcid.org/0000-0002-4746-5791>

**Mahesh Peddigari**

Korea Institute of Materials Science

**Bo Wang**

Pennsylvania State University <https://orcid.org/0000-0003-3146-5559>

**Rui Wang**

Pennsylvania State University

**Woon-Ha Yoon**

Korea Institute of Materials Science

**Jongmoon Jang**

Korea Institute of Materials Science

**Hyunjong Lee**

Korea Institute of Materials Science

**Kyung Song**

Korea Institute of Materials Science <https://orcid.org/0000-0003-3734-1039>

**Geon-Tae Hwang**

Pukyong National University

**Kai Wang**

Pennsylvania State University

**Yuchen Hou**

The Pennsylvania State University

**Haribabu Palneedi**

Pennsylvania State University

**Yongke Yan**

Penn State University

**Han Seung Choi**

Yeungnam University

**Jianjun Wang**

Tsinghua University

**Long-Qing Chen**

The Pennsylvania State University <https://orcid.org/0000-0003-3359-3781>

**Shashank Priya**

Penn State University  
**Dae-Yong Jeong**  
Inha University

---

## Physical Sciences - Article

### Keywords:

**Posted Date:** March 17th, 2022

**DOI:** <https://doi.org/10.21203/rs.3.rs-1411286/v1>

**License:**  This work is licensed under a Creative Commons Attribution 4.0 International License.

[Read Full License](#)

---

# Abstract

Relaxor ferroelectrics (RFEs) are being actively investigated for energy storage applications due to their large electric-field-induced polarization with slim hysteresis and fast energy charging-discharging capability. Here, we report a nanograin engineering approach based upon high kinetic energy deposition for artificially inducing the RFE behavior in a normal ferroelectric  $\text{Pb}(\text{Zr}_{0.52}\text{Ti}_{0.48})\text{O}_3$  (PZT) and simultaneously enhancing the dielectric breakdown strength (EDBS) and polarization. Artificially engineered polycrystalline relaxor PZT films with 4  $\mu\text{m}$  thickness exhibited an exceptional EDBS of 540 MV/m and reduced hysteresis with large unsaturated polarization ( $103.6 \mu\text{C}/\text{cm}^2$ ), resulting in an ultrahigh energy storage density of  $124 \text{ J}/\text{cm}^3$  and a power density of  $64.5 \text{ MW}/\text{cm}^3$ . This fundamental microstructure-based design approach overcomes the limitations imposed by composition and provides a feasible pathway for designing high-performance energy storage materials, where high EDBS, reduced hysteretic behavior, and enhanced polarization are required.

## Main

Relaxor ferroelectrics (RFEs) have attracted significant interest for various applications such as energy storage capacitors, electrocaloric cooling devices, and transducers due to their small polarization (P)–electric field (E) hysteresis, and diffuse phase transition from the ferroelectric (FE) state to the paraelectric (PE) state.<sup>1,2</sup> It is known that these singular characteristics of RFEs originate from polar nanoregions (PNRs), which persist even beyond the FE–PE phase transition as described by Vogel–Fulcher function.<sup>3</sup> As the size of the polar regions in FE materials is reduced to the nanoscale, reaching the critical domain size for exhibiting ferroelectricity, the energy barrier for switching can be significantly lowered, thus exhibiting a high dynamic response to external stimuli such as temperature, electric field, and stress.<sup>4</sup> These distinctive features of RFEs are related to the nanoscale structural heterogeneity, so called ‘polar nano region (PNR)’ resulting from cation order-disorder and the accompanying random electric fields.<sup>5,6</sup> Such inherent compositional and charge inhomogeneities associated with the short-range ordering of cations lead to the natural formation of PNRs/nanodomains within micro-sized grains.<sup>4,7</sup> Current knowledge relies on inducing the RFE characteristics mainly through composition-driven PNR formation. There is no other strategy known for PNR formation that imparts relaxor-like characteristics.

Unlike the traditional composition-driven nanodomains/PNRs, here we propose a microstructure-driven approach for transforming normal FE system to RFE system through formation of nanoscale engineered domain structures. In literature, prior attempts have been made to modify the electrical and structural properties of FE ceramics via mechanical methods such as high-energy neutron/gamma-ray irradiation; however, this energy is insufficient for breaking the microdomains into nanodomains in a ceramic system.<sup>8-10</sup> In soft polymeric FE materials, however, this approach of breaking the uniform microstructure into PNRs has been attempted by Zhang *et al.*, where a normal FE poly(vinylidene fluoride-trifluoroethylene) (P(VDF-TrFE)) copolymer was exposed to high-energy electron irradiation, resulting in the formation of PNRs.<sup>11</sup> Despite the success in the microstructural modification of FE polymers to

induce RFE characteristics, achieving similar transformations in FE ceramics remains extremely challenging owing to the strong ionic bonding.

In this study, we introduce a novel strategy based on nanograin engineering to artificially induce RFE behavior in a normal FE composition, such as lead zirconate titanate ( $\text{Pb}(\text{Zr,Ti})\text{O}_3$ ; PZT). Our approach transforms the long-range ordered microdomains into highly dense short-range ordered nanodomains in the disordered matrix through a high-kinetic-energy deposition technique, aerosol deposition (AD). In AD ceramic films, the presence of a highly disordered nonpolar structure around the crystalline nanodomains within nanograins (induced by the high-speed impact of particles on the substrate) significantly enhances the dielectric breakdown strength ( $E_{\text{DBS}}$ ) and delays the electric field dependent polarization/strain saturation.<sup>12,13</sup> The presence of artificially induced short-range ordered nanodomains that are isolated and equidimensional, *i.e.*, nearly identical grain and domain sizes, in the nonpolar matrix reduces the energy barrier for domain switching.<sup>7</sup> Under these conditions, a higher polarization magnitude under an external field with a slim hysteresis (RFE-like behavior) and enhanced  $E_{\text{DBS}}$  can be simultaneously achieved in polycrystalline form. These artificially engineered RFE capacitors with enhanced  $E_{\text{DBS}}$ , large polarization, and thermal stability have a great potential for replacing the presently used thermally and mechanically unstable polymer-based capacitors.

## Phase-field modeling

To demonstrate the equidimensional nanograin engineering concept for inducing the RFE behavior in ceramic dielectrics, we utilized phase-field simulations on films with different nanograin configurations to understand the electric field endurance limit/distribution and field-induced polarization hysteresis behavior. We simulated a series of PZT microstructures containing the randomly oriented nanograins with volume fractions ranging from 20% to 100% embedded in a nonpolar structure (Fig. 1a and Supplementary Fig. 1) and corresponding equilibrium domain structures under the remnant conditions (Fig. 1b). Further, we applied a unipolar electric field of 400 MV/m and obtained the simulated electric field distributions (Fig. 1c and 1d) and field-dependent polarization hysteresis ( $P$ - $E$ ) loops for each configuration (Fig. 1e). With reduction in the volume fraction of nanograins in the nonpolar matrix, a continuous decrease of the applied electric field magnitude around the nanograins is observed (Fig. 1c and Supplementary Fig. 1),<sup>14-16</sup> which led to enhanced electric field endurance limit and slimming of  $P$ - $E$  loop simultaneously. The simulation results show that the typical features of FE, RFE, and PE are observed for the microstructures with >90%, 60-90%, and <60% nanograin volume fractions, respectively. Although the PE exhibits a relatively higher electric field endurance limit and negligible hysteresis due to the presence of a large fraction of nonpolar structure and reduced nanograin volume fraction, the RFE displays higher field-induced nonlinear polarization than PE and a higher electric field endurance limit than the FE. Thus, RFE is the best choice for achieving high energy storage density as it is related to the maximum applicable electric field (*i.e.*,  $E_{\text{DBS}}$ ), and high electric field-induced polarization (*i.e.* high dielectric permittivity). To quantitatively evaluate the nanograin volume fraction dependent energy storage performance, we estimated the recoverable energy density ( $U_{\text{rec}}$ ) and energy storage efficiency ( $\eta$ )

from the simulated  $P$ - $E$  loops (Supplementary Fig. 2).<sup>3</sup> It is found that the optimum values of  $U_{\text{rec}}$  and  $\eta$  could be achieved with the nanograin volume fractions of 60 to 70 %, however,  $\eta$  shows a monotonic decreasing trend with increasing the nanograin fraction. We found upon further investigation that the nanograin engineered structure, for example, the 60~70 vol.% nanograin volume fraction, exhibits typical RFE features such as slim and nonlinear  $P$ - $E$  hysteresis along with high  $E_{\text{DBS}}$ . However, as the permittivity of the disordered structure ( $\epsilon_a$ ) increases, the electric field distribution around the nanograins increases, leading to the onset of FE behavior (Fig. 1f). Therefore, the key advantage of nanograin engineering with equidimensional grain-domain distribution is that it provides optimum configuration for enhancing the FE functionality as required for energy storage applications. This method relies on the control of the volume fractions of FE nanograins in a nonpolar matrix without modulating the composition.

### **Fabrication of RFE PZT thick films**

The fabrication of highly dense nanograined ceramics with a conventional high temperature sintering process is a challenging task because of the trade-offs between high density and nanoscale grains. In this context, AD enables the fabrication of highly dense nanograined thick ceramic films with a thickness of several microns or more through the fracture of micro-sized primary particles by the high-kinetic-energy and consolidation of the fractured particles at room temperature.<sup>17-20</sup> Unlike the traditional composition-driven RFEs, the AD processing methodology driven artificial RFEs will have negligible compositional heterogeneity and significantly reduced grain boundary defects, which is highly advantageous for operation under high electric fields.

To experimentally demonstrate this approach, we selected a typical normal FE composition, undoped  $\text{Pb}(\text{Zr}_{0.52}\text{Ti}_{0.48})\text{O}_3$ , which usually exhibits square hysteretic behavior due to the presence of long-range FE ordering. We successfully fabricated highly dense nanograined PZT ceramic thick films with RFE behavior using the FE PZT particles through the AD process. The detailed fabrication process is described in the Methods section and the Supplementary Information. We deposited PZT films with a thickness of 4  $\mu\text{m}$  (Supplementary Fig. 3) to overcome the energy density issues in both the bulk and thin film forms.<sup>3</sup> The PZT thick films were annealed at 600  $^\circ\text{C}$  for 1 h and 750  $^\circ\text{C}$  for 4 h to manipulate the volume fractions of the nanodomains and nonpolar structures. The emphasis here is on the annealed (at 600  $^\circ\text{C}$  for 1 h) PZT thick films due to presence of 60-70% nanosized crystallite fraction within nonpolar structure which results in outstanding energy storage properties.

Fig. 2a shows the X-ray diffraction (XRD) patterns of the PZT powder used for the film fabrication and the AD PZT thick films grown on  $\text{Pt}(111)/\text{Ti}/\text{SiO}_2/\text{Si}(100)$  substrates. Both the PZT powder and the thick films were crystallized in a single perovskite phase. The surface and cross-sectional SEM images (Supplementary Fig. 3) of the annealed PZT thick film display a highly dense microstructure with a thickness of  $\sim 4 \mu\text{m}$ . The transmission electron microscopy (TEM) images (Fig. 2b and Supplementary Fig. 3d-e) reveal the presence of equidimensional nano-crystallite domains with a size of  $15 \pm 5 \text{ nm}$ , dispersed in a highly disordered nonpolar matrix having the same composition of nano-crystallite. This microstructure is the result of high-speed collisions between the PZT particles and the substrate during

the AD process, which drives the domain configuration from long-range FE ordering to short-range ordering within a highly disordered nonpolar matrix. The selected area electron diffraction (SAED) pattern (Supplementary Fig. 3f) shows multiple rings with strong (110) reflections confirming the polycrystalline structure, which is consistent with the XRD observations. The arrangement of FE nanodomains in the PZT thick films was characterized using piezo-response force microscopy (PFM). From Supplementary Fig. 4, it can be observed that the as-deposited film contains a high degree of nonpolar disordered structures (indicated in orange) with few randomly oriented nanodomains, where the size, density, and polarization of the nanodomains were substantially enhanced after annealing. Despite the enhanced crystallinity, the annealed PZT film still exhibited a continuous distribution of nonpolar amorphous phase around the crystalline nanodomains, as evidenced by the orange color and diffusive FFT patterns in the PFM amplitude (Supplementary Fig. 4c) and high-resolution TEM (HRTEM) images (Supplementary Fig. 3e), respectively. The obtained microstructure of the annealed AD PZT thick film is in good agreement with our material design strategy (60-70% nanosized crystallite fraction in a nonpolar matrix) and the predictions from the phase-field modeling (Fig. 1). The energy dispersive spectrum (EDS) analysis corroborates that all the elements are homogeneously present in the annealed PZT thick film (Supplementary Fig. 5).

### **The behavior of nanodomains under the influence of electric field**

We performed *in-situ* XRD and TEM analyses to clarify the crystallographic contributions to the macroscopic polarization properties and switching behavior of the nanodomains in the nanograin-engineered PZT thick films (Supplementary Fig. 6). The *in-situ* XRD measurement was performed by collecting the peak profiles of the (200) reflection on the sample surface as a function of the electric field from 0 to 50 MV/m (Fig. 2c and 2d). Interestingly, the (200) peak shows a clear shift towards the lower  $2\theta$  and an increment of 0.27% in the corresponding lattice parameter with increasing electric field, indicating field-induced domain expansion/lattice elongation along the out-of-plane direction. The diffraction peak returned to its initial position after the removal of the electric field without any considerable changes in the intensity or full width at half maximum, indicating the reversible elongation of the pseudocubic unit cell. Further, the dark-field TEM (DF-TEM) images and corresponding SAED patterns were monitored before and after the electric field application to observe the in-plane structural changes in the PZT thick film (Supplementary Fig. 7). From the DF-TEM images, it is ascertained that the brightness and size of the nanodomains were significantly changed after applying the electric field, suggesting changes in the domain orientation. Moreover, the peak positions of the crystal planes, particularly the (100) reflections, were shifted to higher angles with a slightly reduced peak intensity (Supplementary Fig. 7d). At an applied electric field of 50 MV/m, the estimated change in the in-plane lattice parameter is -0.51%. This indicates that the crystal structure distortion via the compression of the in-plane lattice parameter, which is exactly opposite behavior compared to the out-of-plane observation. Such substantial and reversible deformation of the pseudocubic lattice related to the magnitude and direction of the applied electric field helps in achieving a slim hysteresis with an enhanced polarization or strain at high electric fields. In addition, the DC-field dependent PFM analysis also supplements the back-switching behavior of nanodomains (Supplementary Fig. 8). The effective piezoelectric coefficient ( ) of the PZT thick film displays a

significant AC electric field dependent nonlinear behavior with a saturated  $d$  of 157 pm/V (Supplementary Fig. 8e), which could be due to the increased nanodomain density as evidenced from the field-dependent PFM study.

### Electrical and energy storage properties of nanograin-engineered RFE PZT thick film

The temperature- and frequency-dependent dielectric properties were measured to verify the RFE behavior of the nanograin-engineered PZT thick films (Fig. 3a). It is noticed that the PZT thick film exhibited broad and frequency-sensitive dielectric peaks ( $T_m$ ) with a clear shift in the dielectric peaks towards high temperatures of 314 to 334 °C in the frequency range of 100 Hz to 100 kHz, which is a characteristic feature of RFEs. In comparison, the FE PZT ceramic with an average grain size in the micron range exhibited a large dielectric constant maximum with a sharp phase transition at a Curie temperature ( $T_C$ ) of 396 °C without any frequency dispersion (Supplementary Fig. 9). The modified Curie-Weiss law and Vogel-Fulcher equation were adopted to confirm the RFE behavior of nanograin-engineered PZT thick film (Supplementary Figs. 9 and 10). This result demonstrates that the relaxor behavior in FEs can be artificially induced via a mechanical nanograin engineering method beyond any compositional heterogeneity. In addition, the RFE PZT thick film exhibited an ultralow leakage current density of 1.1  $\mu\text{A}/\text{cm}^2$  and an outstanding dielectric tunability of 80.4% at 100 MV/m (Supplementary Figs. 10 and 11).

Because the energy storage capacitors undergo unipolar cycling (charging–discharging) in practice, the unipolar  $P$ – $E$  hysteresis loops for the RFE PZT thick film were measured until the breakdown occurred. A slim  $P$ – $E$  hysteresis with a larger  $DP$  ( $= P_m - P_r$ ) and high  $E_{\text{DBS}}$  are the critical parameters for achieving high energy storage density and efficiency. Interestingly, the nanograin-engineered RFE PZT thick film sustained ultrahigh electric fields of up to 540 MV/m, which is equivalent to the typical  $E_{\text{DBS}}$  of high-performance polymer-based dielectrics<sup>21</sup> and far superior to other ceramic thick films (Supplementary Fig. 12).<sup>7,22-34</sup> Of particular importance is the observation that despite being thick and polycrystalline form, our PZT films exhibited the same  $E_{\text{DBS}}$  level as that of thin epitaxial as well as domain-engineered films and outperformed the polycrystalline films with thickness above 1  $\mu\text{m}$ . Thus, the nanograin engineered thick films meet the standard of practical applications requiring a high energy level due to their high voltage (over 1000 V) endurance capacity and easy fabrication route. The nanograin-engineered RFE PZT thick film also exhibited a slim  $P$ – $E$  hysteresis ( $\Delta P = 75.1 \mu\text{C}/\text{cm}^2$ ) with a large as well as unsaturated  $P_m$  ( $103.6 \mu\text{C}/\text{cm}^2$ ), as shown in Fig. 3b. For instance, we compared the unipolar  $P$ – $E$  loops of three different grain-structured films: as-deposited (highly amorphous), nanograin-engineered, and micrograined (high-temperature annealed) PZT thick films of the same composition as that deposited by AD; the results are depicted in Supplementary Fig. 13. Intriguingly, the PZT thick film with a nanograin-engineered structure exhibited exceptionally higher values of  $E_{\text{DBS}}$  and polarization compared to that of the other films. The large and reversible, field-dependent lattice distortion and enhanced average field strength of the nanodomains in the nonpolar matrix facilitated the synergetic combination of a large  $E_{\text{DBS}}$  and enhanced polarization with a small hysteresis loss, which would greatly enhance the energy storage performance of the PZT thick film. The  $U_{\text{rec}}$  reached a record-breaking value of 124.1

J/cm<sup>3</sup> with a high  $\eta$  of 64% (Fig. 3c) for the nanograin-engineered PZT thick film owing to the optimized microstructure to simultaneously realize a high  $E_{\text{DBS}}$  and polarization. The obtained  $U_{\text{rec}}$  value is many-fold larger than the highly amorphous AD film (35.2 J/cm<sup>3</sup>), micrograined AD film (9.8 J/cm<sup>3</sup>), and other dielectric ceramic thick films (thickness > 1  $\mu\text{m}$ ) reported by other researchers (Fig. 3d).<sup>7,22-34</sup>

### Reliability evaluation and charging–discharging performance of nanograin-engineered RFE PZT thick film capacitors

We analyzed the two-parameter Weibull distribution to estimate the most probable dielectric failure field ( $a$  or characteristic  $E_{\text{DBS}}$ ).<sup>3</sup> For this analysis, the statistical values of  $E_{\text{DBS}}$  were obtained and the distribution was fitted to the Weibull distribution, as shown in Fig. 4a. The artificially induced RFE PZT thick film exhibited an  $a$  value of approximately 487 MV/m (applied voltage of 1950 V), which is still higher than that of the ceramic films having a thickness > 1  $\mu\text{m}$  (Supplementary Fig. 12). The value of  $\beta$  (dispersion in the data) is 4.35, which indicates that the film is homogeneous with the lowest breakdown field of 320 MV/m.

For practical applications, energy storage capacitors must have a longer lifetime and should be able to withstand temperature fluctuations.<sup>3</sup> Therefore, to ensure the reliability of the RFE PZT thick film capacitors, the temperature- and fatigue-cycle-dependent unipolar  $P$ - $E$  loops were measured at an electric field of 200 MV/m (800 V). The relaxor PZT thick film showed a small variation in  $U_{\text{rec}}$  ( $\sim 11.9\%$ ) and  $\eta$  ( $\sim 5.8\%$ ) after  $10^7$  fatigue cycles (Fig. 4b and Supplementary Fig. 14a). Such a high retention of  $U_{\text{rec}}$  and  $\eta$  even after several charging–discharging electric cycles may be due to the less heat generation and dynamic switching behavior of the nanodomains under a cyclic electric field. In addition, the RFE PZT thick film demonstrated excellent temperature stability ( $\Delta U_{\text{rec}} \sim 3.5\%$  and  $\Delta \eta \sim 3\%$ ) in the broad temperature range of 35–150 °C (Fig. 4c and Supplementary Fig. 14b).

A high power density ( $P_{\text{d}}$ ) with a fast discharge time ( $\tau_{0.9}$ ) is another requisite for practical energy storage applications.<sup>21</sup> To evaluate the energy discharge behavior, the PZT thick film capacitor was charged at 250 V ( $\sim 62$  MV/m) and then discharged through the various load resistors ( $R_{\text{L}} \sim 1$ -100 k $\Omega$ ). The values for  $U_{\text{rec}}$  and  $P_{\text{d}}$  were calculated using the voltage decay profile (Supplementary Fig. 14c). At an  $R_{\text{L}}$  of 1 k $\Omega$ , the RFE PZT thick film exhibited a maximum  $U_{\text{rec}}$  of 8.44 J/cm<sup>3</sup>, a superior instantaneous  $P_{\text{d}}$  of 64.5 MW/cm<sup>3</sup>, and an ultrafast  $\tau_{0.9}$  of 290 ns (Fig. 4d and Supplementary Fig. 14d), which is an excellent match for pulsed power applications. Moreover, the  $U_{\text{rec}}$  is improved with increasing the  $R_{\text{L}}$  while the  $P_{\text{d}}$  is decreased due to delayed charge transfer.

These results demonstrate that the fabrication of artificially tailored RFE ceramic thick films with equidimensional nanograins and domain structures via nanograin engineering is an efficient way to achieve ultrahigh energy storage properties. It was confirmed that the AD technique provides highly dense RFE thick films with nanosized grains. Such microstructure realization is beyond the capabilities of

traditional composition modification approaches. We believe that these transformative results will have a significant impact on the development of high energy storage density capacitors.

## Conclusions

In summary, a nanograin engineering approach for inducing artificial RFE behavior in normal FEs was demonstrated by controlling the amount of nanograins and nonpolar structures. Using this emerging approach, which provides nanostructures beyond that of known methods based upon compositional modulation, a record-breaking energy storage density of  $124.1 \text{ J/cm}^3$  under an exceptionally high electric field of  $540 \text{ MV/m}$  (over  $2000 \text{ V}$ ) was realized in a  $4 \text{ }\mu\text{m}$  thick RFE PZT film with equidimensional nanograins and domain structure. As this approach is based on the engineering of nanodomains without any compositional modification or complex processing, it holds great promise for inducing high-temperature RFE behavior and improving the energy storage performance of dielectrics, as well as the performance of other functional materials with specific application requirements.

## Methods

### Preparation of PZT powders

Lead zirconate titanate powders of  $\text{Pb}(\text{Zr}_{0.52}\text{Ti}_{0.48})\text{O}_3$  were prepared using a conventional solid-state reaction method. Stoichiometric amounts of  $\text{PbO}$ ,  $\text{ZrO}_2$ , and  $\text{TiO}_2$  (with a purity  $> 99.9 \%$ , M/s Sigma-Aldrich) powders were mixed by ball-milling for 24 h in a high-density polyethylene jar with stabilized  $\text{ZrO}_2$  balls and anhydrous ethanol as the grinding media. The obtained slurry was dried at  $80 \text{ }^\circ\text{C}$  using a rotary evaporator (N-1300, EYELA) and further calcined at  $850 \text{ }^\circ\text{C}$  for 4 h to induce the single-phase perovskite PZT phase.

### Deposition of PZT thick films

Before the deposition, the calcined powders were again ball-milled for 24 h and heat-treated at  $500 \text{ }^\circ\text{C}$  for 2 h to obtain a proper particle size distribution for the AD process. These powders were sieved and mixed with a carrier gas (medical grade dried air) to form an aerosol. A Laval-type nozzle with a rectangular orifice ( $10 \times 0.5 \text{ mm}^2$ ) was used to feed the particles into the vacuum chamber. The processing parameters such as the particle suspension feed rate ( $12 \text{ L/min}$ ), scan speed ( $1 \text{ mm/s}$ ), and repetitions (10 cycles) were optimized to obtain a PZT film thickness of  $4 \text{ }\mu\text{m}$  on a  $\text{Pt}(111)/\text{Ti}/\text{SiO}_2/\text{Si}(100)$  substrate. Furthermore, the PZT thick films were annealed at  $600 \text{ }^\circ\text{C}$  for 1 h and  $750 \text{ }^\circ\text{C}$  for 4 h (the heating and cooling rates were  $1 \text{ }^\circ\text{C}$  and  $0.5 \text{ }^\circ\text{C}$ , respectively) to improve the density, crystallinity, and grain size. Moreover, PZT pellets were fabricated using the same powder and sintered at  $1220 \text{ }^\circ\text{C}$  for 2 h to compare the results with the thick films.

### Characterization

The phase purity of the PZT powders and thick films was investigated using X-ray diffraction (XRD; D-MAX 2500, Rigaku) with Cu K<sub>α</sub> radiation ( $\lambda = 0.1506$  nm). Scanning electron microscopy (SEM; JSM-5800, JEOL) and transmission electron microscopy (TEM; JEM-2100F, JEOL) were used to observe the microstructure of the thick film. The electric-field-dependent domain response was observed using an *in-situ* TEM system (JEM-2100, JEOL). The electric-field-dependent XRD profiles were obtained using a high-resolution XRD (X'Pert<sup>3</sup> MRD, Malvern Panalytical) equipped with a DC power supply (Keithley, 2290–5) and a homemade fixture. The FE domain structures of the PZT thick films were obtained using piezoelectric response microscopy (PFM, Innova AFM, BRUKER) in the tapping mode by varying the DC bias from 0 to 9 V at an AC voltage amplitude of 5 V. For electrical measurements, circular (diameter of 0.5–1 mm) and rectangular ( $5 \times 10$  mm<sup>2</sup>) Pt electrodes were deposited on the PZT thick film using a DC sputtering system (108, Cressington). The frequency (100 Hz to 100 kHz) and temperature (25–600 °C) -dependent dielectric properties were measured using an RF impedance analyzer (4284, HP) and a high-temperature electric probe system (LABSYS HTEP-8000, Nextron). The temperature-dependent (25–150 °C) FE hysteresis loops were recorded at 1 kHz using a ferroelectric tester (Precision LC-II, Radiant Technologies) by placing the specimen on a hot chuck. The leakage current characteristics were measured using a multimeter (2611A, Keithley). The time-dependent charge–discharge profiles were measured using a homemade high-speed switching circuit and an oscilloscope (WaveSurfer 44Xs-A, LeCroy).

### Phase-field simulations

The phase-field methods were comprehensively employed to establish the nanograined and micrograined structures of the PZT films and simulate the formation and evolution of domain structures in the films under a zero electric field and during the unipolar poling process. There are mainly three steps in the procedure. First, the phase-field method for grain growth was used to generate a series of nanograined structures with different volume fractions (from 22% to nearly 100%) by controlling the number of initial seeds and the simulation time.<sup>35</sup> The grains separated by grain boundaries are treated as the crystalline phase of PZT while the untransformed regions are regarded as the amorphous phase. The grain boundaries are treated as diffuse interfaces whose properties are linearly interpolated between those of the adjacent crystalline or amorphous phases. As known from the experiments, the nanocrystalline regions of PZT exhibit a random distribution of the crystallographic orientation. Therefore, we assigned to each grain *i* a random orientation characterized by three Euler angles,  $\theta$ ,  $\phi$ , and  $\psi$  that corresponds to the "Z-X'-Z" convention. Second, we employed the phase-field model for an inhomogeneous ferroelectric to obtain the polarization distribution at equilibrium in the as-grown state by quenching the system to 300K with a small random distribution of polarization.<sup>36</sup> Considering  $\sim 4$   $\mu\text{m}$  thickness of the PZT films, the surface and substrate effects can be neglected. Therefore, we modelled the system as a stress-free bulk system using three-dimensional periodic boundary conditions. Finally, for each structure, we applied a unipolar electric field with a one-cycle triangular waveform and a maximal field strength to obtain the unipolar *P-E* hysteresis loop. The rate of the applied field is assumed to be slow to obtain the quasi-static response.

The bulk system is discretized into  $420\Delta x \times 160\Delta y \times 1\Delta z$  grid points with real grid spaces  $\Delta x = \Delta y = \Delta z = 1$  nm. A dimensionless time step of  $\Delta t = 0.01$  is used for solving the time-dependent Ginzburgh-Landau

$$\frac{\partial \mathbf{P}(\mathbf{x}, t)}{\partial t} = -L \frac{\delta F}{\delta \mathbf{P}(\mathbf{x}, t)}, \text{ where } \mathbf{P}(\mathbf{x}, t)$$

equation for the polarization evolution, i.e.,

is the spatial-temporal field of the polarization vector,  $L$  the kinetic coefficient, and  $F$  is the total free energy, which can be obtained by integrating the bulk chemical energy density ( $f_{\text{bulk}}$ ), elastic energy density ( $f_{\text{elastic}}$ ), electrical energy density ( $f_{\text{electric}}$ ), and polarization gradient energy density ( $f_{\text{grad}}$ ) over the whole system according to the following equation:

$$F = \iiint_V (f_{\text{bulk}} + f_{\text{elastic}} + f_{\text{electric}} + f_{\text{grad}}) dV. \quad (4)$$

The detailed expressions of these energy densities can be found in earlier works.<sup>36</sup> For relaxational simulation under zero electric field, a total timestep of 10,000 is sufficient to obtain the equilibrium polarization configuration. For modeling the unipolar poling process, an applied external electric field is applied along the  $y$  axis which increases linearly from zero to  $E_m$  in the first 50,000 timesteps and linearly decreases to zero in the next. The detailed formulation and numerical implementations of the phase-field models for grain growth and ferroelectric materials have been documented in earlier works.<sup>35,37</sup> For bulk systems with periodic boundary conditions, the mechanical and electrostatic energies can be conveniently solved in the reciprocal space using the spectral method,<sup>37</sup> while the inhomogeneity of mechanical and dielectric properties associated with the crystalline and amorphous phases can be considered by using the Fourier-spectral iterative perturbation method.<sup>36</sup> The materials parameters were taken from literatures for  $\text{PbZr}_{1-x}\text{Ti}_x\text{O}_3$  with the mole fraction of Ti as  $x = 0.48$ .<sup>38</sup> The gradient energy coefficient  $g_{ij}$  is assumed to be isotropic with a normalized value of 0.6 which gives a domain wall width of 1 – 2 nm.

## Data and materials availability

All the data presented in the article and Supplementary Material are available from the corresponding authors upon reasonable request.

## References

- 1 Zhao, P. *et al.* High-Performance Relaxor Ferroelectric Materials for Energy Storage Applications. *Adv. Energy. Mater.* **9**, 1803048, (2019).
- 2 Kim, J. *et al.* Ultrahigh capacitive energy density in ion-bombarded relaxor ferroelectric films. *Science* **369**, 81-84, (2020).

- 3 Palneedi, H., Peddigari, M., Hwang, G.-T., Jeong, D.-Y. & Ryu, J. High-Performance Dielectric Ceramic Films for Energy Storage Capacitors: Progress and Outlook. *Adv. Func. Mater.* **28**, 1803665, (2018).
- 4 Lv, X., Zhang, X.-x. & Wu, J. Nano-domains in lead-free piezoceramics: a review. *J. Mater. Chem. A* **8**, 10026-10073, (2020).
- 5 Li, F. *et al.* The origin of ultrahigh piezoelectricity in relaxor-ferroelectric solid solution crystals. *Nat. Comm.* **7**, 13807, (2016).
- 6 Li, F., Zhang, S., Damjanovic, D., Chen, L.-Q. & Shrout, T. R. Local Structural Heterogeneity and Electromechanical Responses of Ferroelectrics: Learning from Relaxor Ferroelectrics. *Adv. Func. Mater.* **28**, 1801504, (2018).
- 7 Pan, H. *et al.* Ultrahigh–energy density lead-free dielectric films via polymorphic nanodomain design. *Science* **365**, 578-582, (2019).
- 8 Hilczer, B. Effect of neutron irradiation on the ferroelectric properties of barium titanate ceramics. *physica status solidi (b)* **2**, 447-455, (1962).
- 9 Kobayashi, S. Effect of neutron irradiation on dielectric properties of barium titanate ceramics. *Electr. Eng. Jpn.* **94**, 15-20, (1974).
- 10 Medhi, N. & Nath, A. K. Gamma Ray Irradiation Effects on the Ferroelectric and Piezoelectric Properties of Barium Titanate Ceramics. *J. Mater. Eng. Perform.* **22**, 2716-2722, (2013).
- 11 Zhang, Q. M., Bharti, V. & Zhao, X. Giant Electrostriction and Relaxor Ferroelectric Behavior in Electron-Irradiated Poly(vinylidene fluoride-trifluoroethylene) Copolymer. *Science* **280**, 2101-2104, (1998).
- 12 Cai, Z. *et al.* Grain-size–dependent dielectric properties in nanograin ferroelectrics. *J. Am. Ceram. Soc.* **101**, 5487-5496, (2018).
- 13 Exner, J., Nazarenus, T., Hanft, D., Kita, J. & Moos, R. What Happens during Thermal Post-Treatment of Powder Aerosol Deposited Functional Ceramic Films? Explanations Based on an Experiment-Enhanced Literature Survey. *Adv. Mater* **32**, 1908104, (2020).
- 14 Liu, N., Su, Y. & Weng, G. J. A phase-field study on the hysteresis behaviors and domain patterns of nanocrystalline ferroelectric polycrystals. *J. Appl. Phys.* **113**, 204106, (2013).
- 15 Xie, J. *et al.* Achieving ultrahigh energy storage performance in bismuth magnesium titanate film capacitors via amorphous-structure engineering. *J. Mater. Chem. C* **7**, 13632-13639, (2019).
- 16 Grabowski, C. A. *et al.* Dielectric Breakdown in Silica–Amorphous Polymer Nanocomposite Films: The Role of the Polymer Matrix. *ACS Appl. Mater. Interfaces* **5**, 5486-5492, (2013).

- 17 Akedo, J., Park, J.-H. & Kawakami, Y. Piezoelectric thick film fabricated with aerosol deposition and its application to piezoelectric devices. *Jpn. J. Appl. Phys.* **57**, 07LA02, (2018).
- 18 Ryu, J. *et al.* Fabrication and ferroelectric properties of highly dense lead-free piezoelectric ( $\text{K}_{0.5}\text{Na}_{0.5}$ ) $\text{NbO}_3$  thick films by aerosol deposition. *Appl. Phys. Lett.* **90**, 152901, (2007).
- 19 Hwang, G.-T. *et al.* Self-Powered Wireless Sensor Node Enabled by an Aerosol-Deposited PZT Flexible Energy Harvester. *Adv. Energy. Mater.* **6**, 1600237, (2016).
- 20 Palneedi, H. *et al.* Unleashing the Full Potential of Magnetoelectric Coupling in Film Heterostructures. *Adv. Mater* **29**, 1605688, (2017).
- 21 Chu, B. *et al.* A Dielectric Polymer with High Electric Energy Density and Fast Discharge Speed. *Science* **313**, 334-336, (2006).
- 22 Pan, H. *et al.* Giant energy density and high efficiency achieved in bismuth ferrite-based film capacitors via domain engineering. *Nat. Comm.* **9**, 1813, (2018).
- 23 Pan, H. *et al.* Ultrahigh energy storage in superparaelectric relaxor ferroelectrics. *Science* **374**, 100-104, (2021).
- 24 Cheng, H. *et al.* Demonstration of ultra-high recyclable energy densities in domain-engineered ferroelectric films. *Nat. Comm.* **8**, 1999, (2017).
- 25 Sun, N., Li, Y., Zhang, Q. & Hao, X. Giant energy-storage density and high efficiency achieved in ( $\text{Bi}_{0.5}\text{Na}_{0.5}$ ) $\text{TiO}_3$ - $\text{Bi}(\text{Ni}_{0.5}\text{Zr}_{0.5})\text{O}_3$  thick films with polar nanoregions. *J. Mater. Chem. C* **6**, 10693-10703, (2018).
- 26 Wang, J. *et al.* Effects of  $\text{Fe}^{3+}$  doping on electrical properties and energy-storage performances of the ( $\text{Na}_{0.85}\text{K}_{0.15}$ ) $_{0.5}\text{Bi}_{0.5}\text{TiO}_3$  thick films prepared by sol-gel method. *J. Alloy. Compd* **727**, 596-602, (2017).
- 27 Wang, J. *et al.* Effects of Mn doping on dielectric properties and energy-storage performance of  $\text{Na}_{0.5}\text{Bi}_{0.5}\text{TiO}_3$  thick films. *Ceram. Int.* **43**, 7804-7809, (2017).
- 28 Liu, Y., Hao, X. & An, S. Significant enhancement of energy-storage performance of ( $\text{Pb}_{0.91}\text{La}_{0.09}$ ) ( $\text{Zr}_{0.65}\text{Ti}_{0.35}$ ) $\text{O}_3$  relaxor ferroelectric thin films by Mn doping. *J. Appl. Phys.* **114**, 174102, (2013).
- 29 Gao, H., Hao, X., Zhang, Q., An, S. & Kong, L. B. Electrocaloric effect and energy-storage performance in grain-size-engineered PBLZT antiferroelectric thick films. *J. Mater. Sci. Mater. Electron.* **27**, 10309-10319, (2016).
- 30 Gao, H. *et al.* Enhanced electrocaloric effect and energy-storage performance in PBLZT films with various  $\text{Ba}^{2+}$  content. *Ceram. Int.* **42**, 16439-16447, (2016).

- 31 Hao, X., Wang, Y., Zhang, L., Zhang, L. & An, S. Composition-dependent dielectric and energy-storage properties of (Pb,La)(Zr,Sn,Ti)O<sub>3</sub> antiferroelectric thick films. *Appl. Phys. Lett.* **102**, 163903, (2013).
- 32 Ma, B. *et al.* PLZT film capacitors for power electronics and energy storage applications. *J. Mater. Sci. Mater. Electron.* **26**, 9279-9287, (2015).
- 33 Wang, Y., Hao, X., Yang, J., Xu, J. & Zhao, D. Fabrication and energy-storage performance of (Pb,La)(Zr,Ti)O<sub>3</sub> antiferroelectric thick films derived from polyvinylpyrrolidone-modified chemical solution. *J. Appl. Phys.* **112**, 034105, (2012).
- 34 Peddigari, M. *et al.* Boosting the Recoverable Energy Density of Lead-Free Ferroelectric Ceramic Thick Films through Artificially Induced Quasi-Relaxor Behavior. *ACS Appl. Mater. Interfaces* **10**, 20720-20727, (2018).
- 35 Fan, D. & Chen, L. Q. Computer simulation of grain growth using a continuum field model. *Acta Mater.* **45**, 611-622, (1997).
- 36 Wang, J. J., Ma, X. Q., Li, Q., Britson, J. & Chen, L.-Q. Phase transitions and domain structures of ferroelectric nanoparticles: Phase field model incorporating strong elastic and dielectric inhomogeneity. *Acta Mater.* **61**, 7591-7603, (2013).
- 37 Hu, H.-L. & Chen, L.-Q. Three-Dimensional Computer Simulation of Ferroelectric Domain Formation. *J. Am. Ceram. Soc.* **81**, 492-500, (1998).
- 38 Haun, M. J., Zhuang, Z. Q., Furman, E., Jang, S. J. & Cross, L. E. Thermodynamic theory of the lead zirconate-titanate solid solution system, part III: Curie constant and sixth-order polarization interaction dielectric stiffness coefficients. *Ferroelectr.* **99**, 45-54, (1989).

## Declarations

### Acknowledgments

This work was supported by National Research Foundation of Korea (grant number NRF-2019R1A2B5B01070100). H.P. and S.P. acknowledge the financial support through DARPA TE3 program (award number: W911NF1620010). Y.Y. acknowledges the financial support through NSF DMR program (award number: 1936432). Y.H. and K.W. acknowledge the financial support through AFOSR Biophysics program (award number FA9550-20-1-0157). M.P., W.-H.Y, and J.J acknowledge the financial support provided by a National Research Council of Science & Technology (NST) grant by the Korean government (MSIP) (No. CAP-17-04-KRISS) and the Korea Institute of Materials Science Internal R&D program (No. PNK7560).

## Author information

### Affiliations

**Department of Functional Ceramics, Korea Institute of Materials Science (KIMS); Changwon, Gyeongnam 51508, Republic of Korea.**

Mahesh Peddigari, Woon-Ha Yoon, and Jongmoon Jang

**Materials Research Institute/Department of Materials Science and Engineering, Pennsylvania State University; University Park, PA 16802, USA.**

Bo Wang, Rui Wang, Kai Wang, Yuchen Hou, Haribabu Palneedi, Yong Ke Yan, Jianjun Wang, Long-Qing Chen, and Shashank Priya

**Department of Materials Analysis and Evaluation, Korea Institute of Materials Science (KIMS); Changwon, Gyeongnam 51508, Republic of Korea.**

Hyunjong Lee, and Kyung Song

**Department of Materials Science and Engineering, Pukyong National University; Busan 43241, Republic of Korea.**

Geon-Tae Hwang

**School of Materials Science and Engineering, Yeungnam University; Gyeongsan, Gyeongbuk 38541, Republic of Korea.**

Han Seung Choi, and Jungho Ryu

**Department of Materials Science and Engineering, Inha University; Incheon 22212, Republic of Korea.**

Dae-Yong Jeong

**Institute of Materials Technology, Yeungnam University; Gyeongsan, Gyeongbuk 38541, Republic of Korea.**

Jungho Ryu

### Contributions

M.P., S.P., D.-Y.J., and J.R. jointly conceived the research and wrote the manuscript. M.P. fabricated the AD thick films, collected the preliminary data (XRD, SEM, HRTEM, dielectric, and ferroelectric data), and analyzed the results with the help of W.-H.Y., J.J., and G.-T.H. *In-situ* TEM measurements were performed by H.L. and K.S. PFM measurements were performed by K.W. and Y.H. *In-situ* XRD measurements were

conducted by H.P, H.S.C., and Y.K.Y. Phase-field simulations were performed by B.W., J.W. and L.-Q.C. The project was supervised by J.R.

Corresponding authors

Correspondence to Shashank Priya, Dae-Yong Jeong, and Jungho Ryu

Email: [sup103@psu.edu](mailto:sup103@psu.edu), [dyjeong@inha.ac.kr](mailto:dyjeong@inha.ac.kr), [jhryu@ynu.ac.kr](mailto:jhryu@ynu.ac.kr)

## **Ethics declarations**

Competing interests

The authors declare no competing interests.

## **Figures**

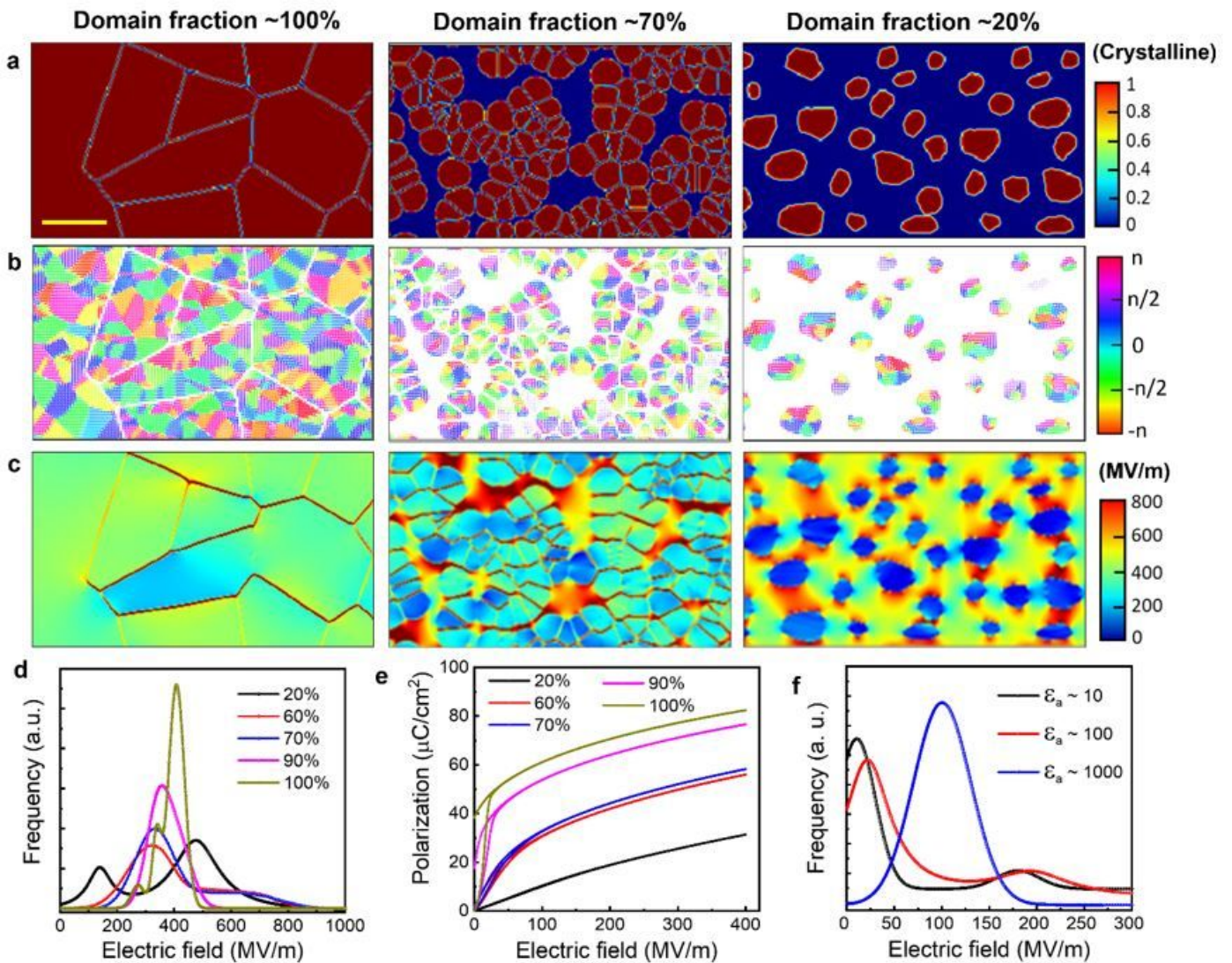


Figure 1

**Nanograin engineering approach for inducing the artificial RFE behavior with enhanced breakdown strength in normal FEs.** **a–f**, Phase-field simulation results for understanding the polarization and electric field endurance behavior of polycrystalline FE materials with various nanograin volume fractions. **a**, **b**, and **c** show the simulated micrographs, corresponding domain structures in the unpoled state, and electric field distribution under an electric field of 400 MV/m of the randomly oriented polycrystalline FE materials with various nanograin volume fractions, respectively. **d** and **e**, Simulated electric field distribution histogram results and  $P$ – $E$  loops obtained at 400 MV/m. **f** shows the electric field distribution histogram results for 60% nanograin volume fraction specimen estimated as a function of the dielectric constant of the disordered structure/matrix ( $\epsilon_a$ ) at 100 MV/m. The dimensions of all micrographs are 270  $\times$  160 nm<sup>2</sup> and the yellow scalebar in **a** is approximately 50 nm.

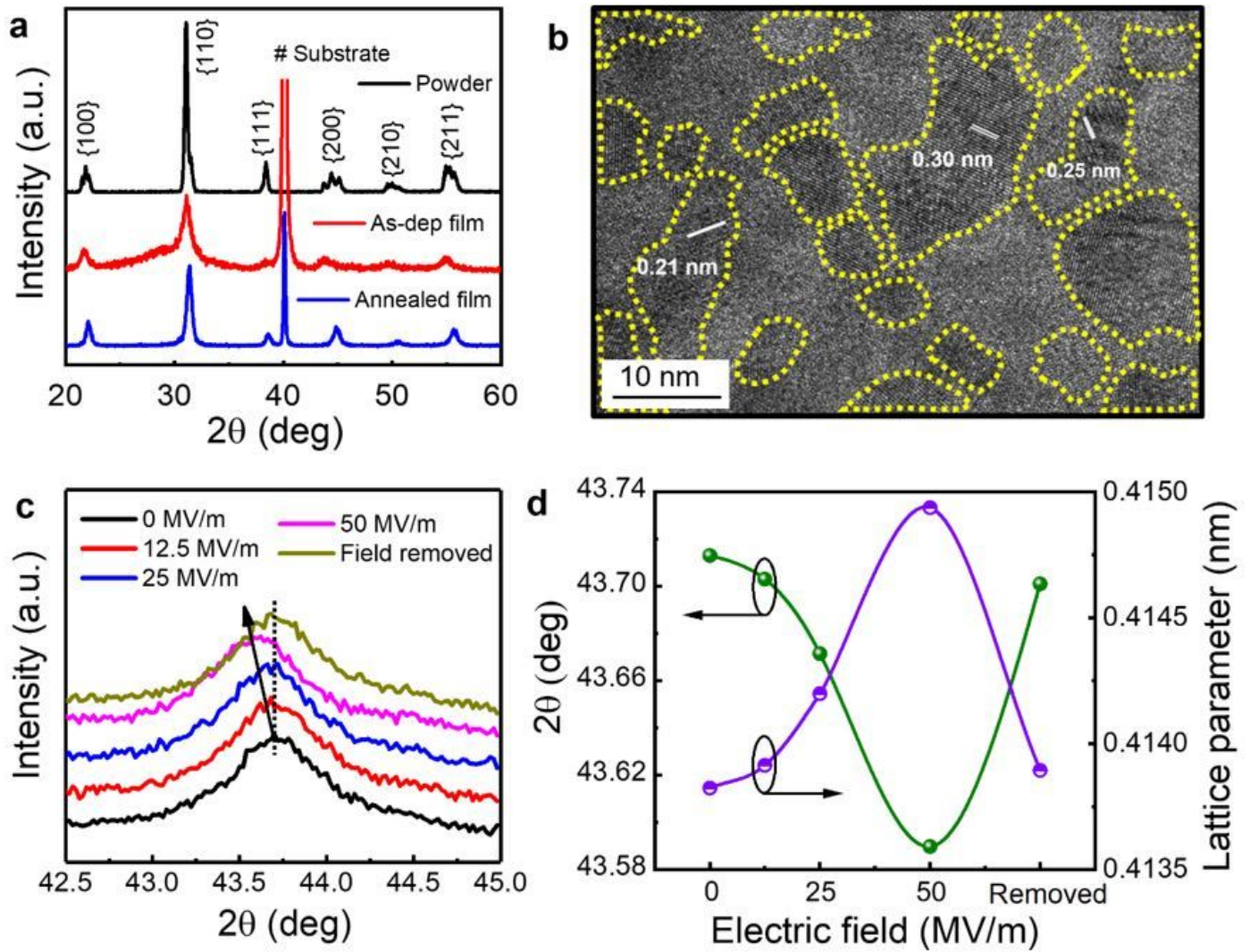
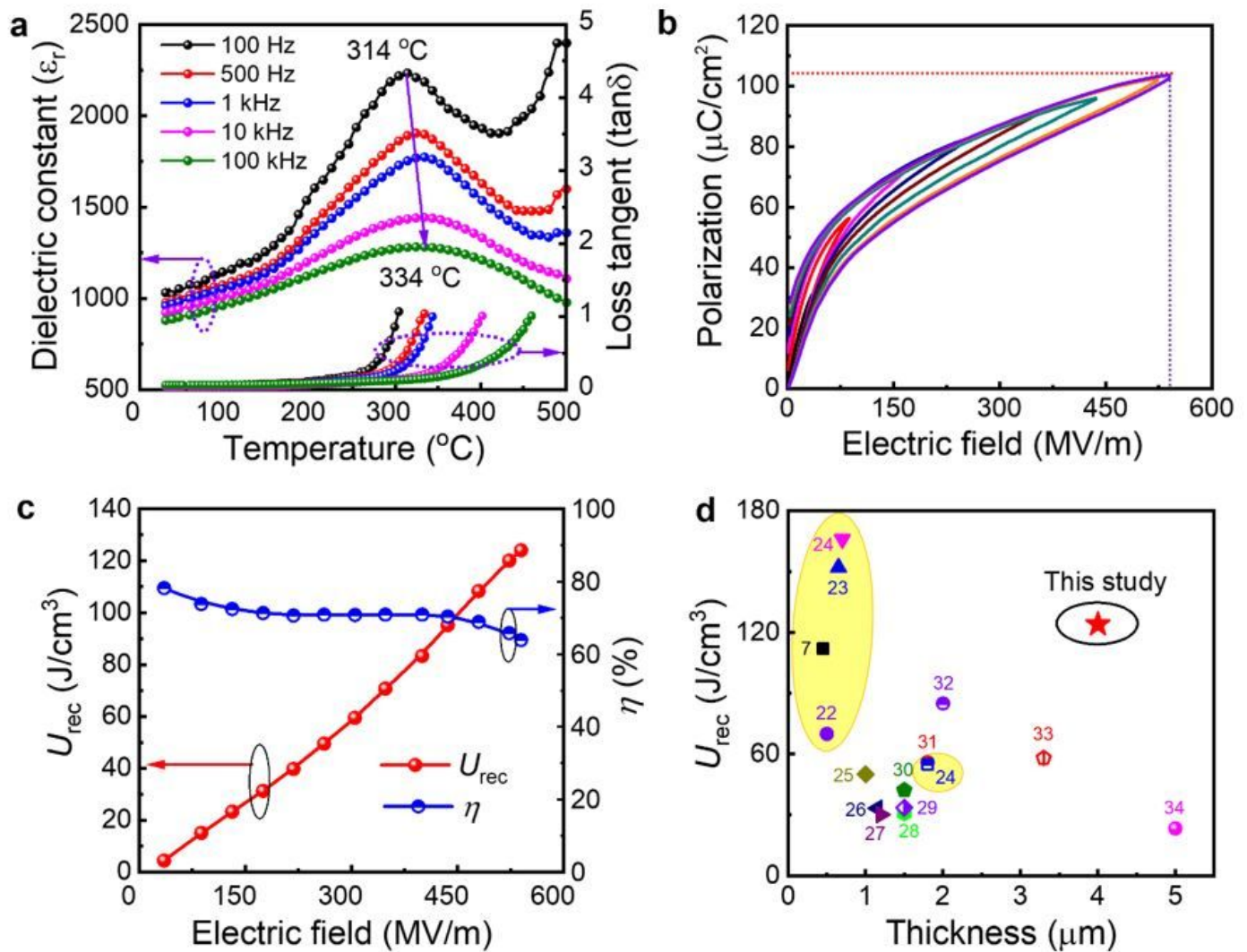


Figure 2

**The behavior of nanodomains under the influence of electric field via *in-situ* observation.** **a**, XRD patterns of the calcined PZT powder, and as-deposited and annealed (at 600 °C for 1 h) films. **b**, HRTEM image of PZT thick film, where nanodomains with various interplanar spacings are visible (areas highlighted with yellow dash lines indicate the nanodomains). **c-d**, *in-situ* XRD measurement showing the out-of-plane structural changes in the nanograin-engineered PZT thick film. **c**, XRD patterns of the PZT (200) peak obtained at different electric fields. **d**, Variations in the PZT (200) peak position and lattice parameter as a function of the electric field.



**Figure 3**

**Electrical and energy storage properties of nanograin-engineered PZT thick film.** **a**, Temperature-dependent dielectric properties ( $\epsilon_r$  and  $\tan\delta$ ) of the PZT thick film measured at various frequencies (100 Hz to 100 kHz), displaying the diffused phase transition around the Curie temperature with  $\Delta T$  of 20 °C. **b**, Unipolar  $P$ - $E$  loops of nanograin-engineered PZT thick film measured up to the breakdown field at a frequency of 1 kHz. **c**, Recoverable energy density and energy storage efficiency as a function of the electric field estimated using the unipolar  $P$ - $E$  loops. **d**, Comparison of the recoverable energy density of the PZT thick film capacitor with other state-of-the-art dielectric capacitors having a thickness  $> 0.4 \mu\text{m}$ . The symbols in the yellow circles represent the domain engineered epitaxial films, while the other symbols represent the polycrystalline films.

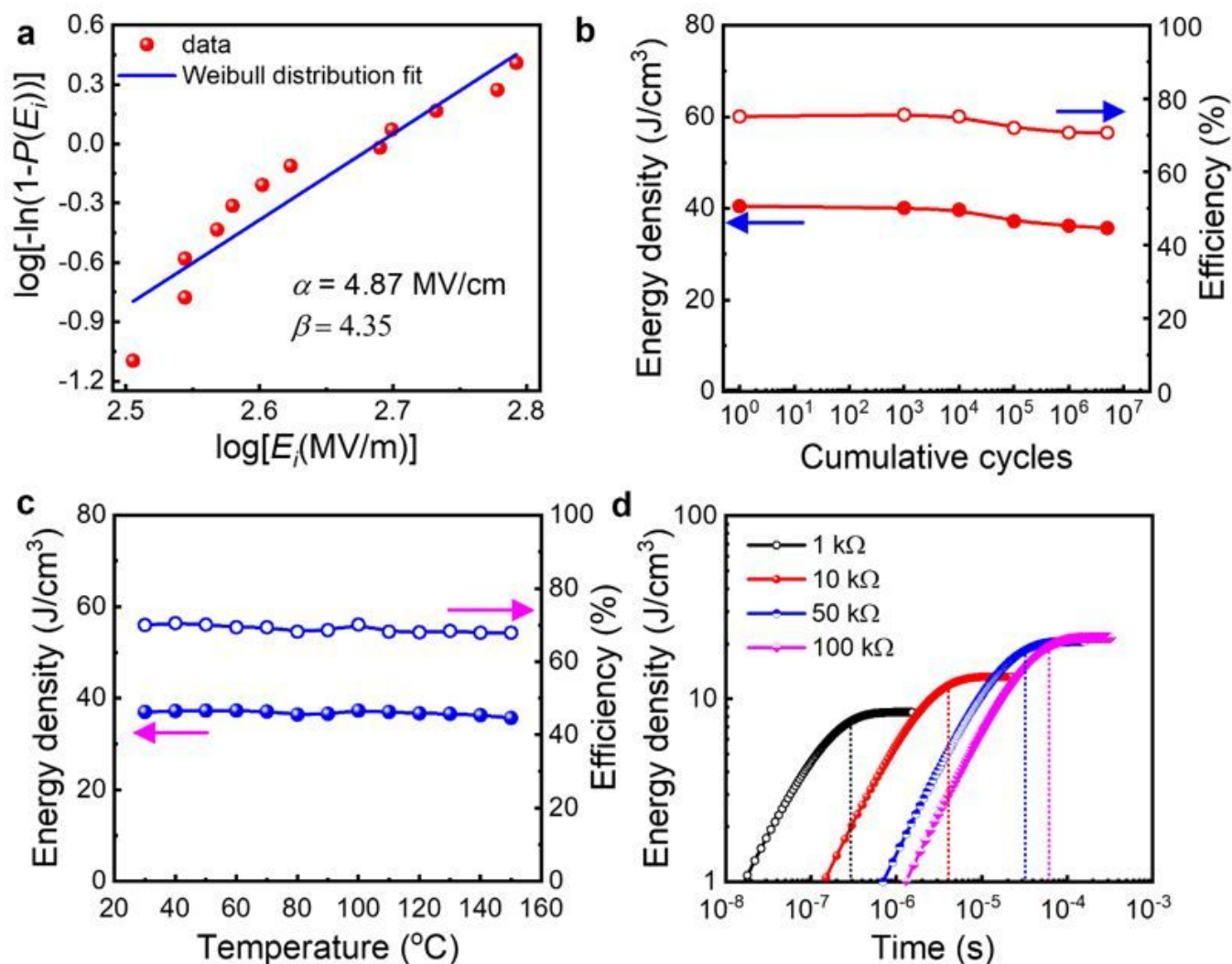


Figure 4

**Reliability evaluation and charging–discharging performance of nanograin-engineered RFE PZT thick film.** **a**, Weibull distribution for estimating the most probable dielectric breakdown field for the PZT thick film. The film displayed **b**, excellent fatigue endurance behavior up to  $10^7$  electric cycles and **c**, good thermal stability up to  $150\text{ }^\circ\text{C}$  at  $E = 200\text{ MV/m}$ . **d**, Pulse discharge properties of RFE PZT thick film capacitor. Time-dependent discharged energy density of RFE PZT thick film capacitor measured at  $250\text{ V}$  as a function of load resistances.

## Supplementary Files

This is a list of supplementary files associated with this preprint. Click to download.

- [SupplementaryInformation20220302.docx](#)